DESY 97-025 ISSN 0418-9833

Comparison of ZEUS Data with Standard Model Predictions for $e^+p \to e^+X$ Scattering at High x and Q^2

ZEUS Collaboration

Abstract

Using the ZEUS detector at HERA, we have studied the reaction $e^+p \to e^+X$ for $Q^2 > 5000\,\mathrm{GeV}^2$ with a $20.1\,\mathrm{pb}^{-1}$ data sample collected during the years 1994 to 1996. For Q^2 below $15000\,\mathrm{GeV}^2$, the data are in good agreement with Standard Model expectations. For $Q^2 > 35000$ GeV^2, two events are observed while 0.145 ± 0.013 events are expected. A statistical analysis of a large ensemble of simulated Standard Model experiments indicates that with probability 6.0%, an excess at least as unlikely as that observed would occur above *some* Q^2 cut. For $x > 0.55$ and $y > 0.25$, four events are observed where 0.91 ± 0.08 events are expected. A statistical analysis of the two-dimensional distribution of the events in x and y yields a probability of 0.72% for the region $x > 0.55$ and $y > 0.25$ and a probability of 7.8% for the entire $Q^2 > 5000\,\mathrm{GeV}^2$ data sample. The observed excess above Standard Model expectations is particularly interesting because it occurs in a previously unexplored kinematic region.

To be published in Zeitschrift für Physik C.

The ZEUS Collaboration

J. Breitweg, M. Derrick, D. Krakauer, S. Magill, D. Mikunas, B. Musgrave, J. Repond, R. Stanek, R.L. Talaga, R. Yoshida, H. Zhang
Argonne National Laboratory, Argonne, IL, USA [p]

M.C.K. Mattingly
Andrews University, Berrien Springs, MI, USA

F. Anselmo, P. Antonioli, G. Bari, M. Basile, L. Bellagamba, D. Boscherini, A. Bruni, G. Bruni, G. Cara Romeo, G. Castellini[1], L. Cifarelli[2], F. Cindolo, A. Contin, M. Corradi, S. De Pasquale, I. Gialas[3], P. Giusti, G. Iacobucci, G. Laurenti, G. Levi, A. Margotti, T. Massam, R. Nania, F. Palmonari, A. Pesci, A. Polini, G. Sartorelli, Y. Zamora Garcia[4], A. Zichichi
University and INFN Bologna, Bologna, Italy [f]

C. Amelung, A. Bornheim, I. Brock, K. Coböken, J. Crittenden, R. Deffner, M. Eckert, L. Feld[5], M. Grothe, H. Hartmann, K. Heinloth, L. Heinz, E. Hilger, H.-P. Jakob, U.F. Katz, E. Paul, M. Pfeiffer, Ch. Rembser, J. Stamm, R. Wedemeyer[6]
Physikalisches Institut der Universität Bonn, Bonn, Germany [c]

D.S. Bailey, S. Campbell-Robson, W.N. Cottingham, B. Foster, R. Hall-Wilton, M.E. Hayes, G.P. Heath, H.F. Heath, D. Piccioni, D.G. Roff, R.J. Tapper
H.H. Wills Physics Laboratory, University of Bristol, Bristol, U.K. [o]

M. Arneodo[7], R. Ayad, M. Capua, A. Garfagnini, L. Iannotti, M. Schioppa, G. Susinno
Calabria University, Physics Dept.and INFN, Cosenza, Italy [f]

J.Y. Kim, J.H. Lee, I.T. Lim, M.Y. Pac[8]
Chonnam National University, Kwangju, Korea [h]

A. Caldwell[9], N. Cartiglia, Z. Jing, W. Liu, J.A. Parsons, S. Ritz[10], S. Sampson, F. Sciulli, P.B. Straub, Q. Zhu
Columbia University, Nevis Labs., Irvington on Hudson, N.Y., USA [q]

P. Borzemski, J. Chwastowski, A. Eskreys, Z. Jakubowski, M.B. Przybycień, M. Zachara, L. Zawiejski
Inst. of Nuclear Physics, Cracow, Poland [j]

L. Adamczyk, B. Bednarek, K. Jeleń, D. Kisielewska, T. Kowalski, M. Przybycień, E. Rulikowska-Zarębska, L. Suszycki, J. Zając
Faculty of Physics and Nuclear Techniques, Academy of Mining and Metallurgy, Cracow, Poland [j]

Z. Duliński, A. Kotański
Jagellonian Univ., Dept. of Physics, Cracow, Poland [k]

G. Abbiendi[11], L.A.T. Bauerdick, U. Behrens, H. Beier, J.K. Bienlein, G. Cases, O. Deppe, K. Desler, G. Drews, D.J. Gilkinson, C. Glasman, P. Göttlicher, J. Große-Knetter, T. Haas, W. Hain, D. Hasell, H. Heßling, Y. Iga, K.F. Johnson[12], M. Kasemann, W. Koch, U. Kötz, H. Kowalski, J. Labs, L. Lindemann, B. Löhr, M. Löwe[13], J. Mainusch[14], O. Mańczak, J. Milewski, T. Monteiro[15], J.S.T. Ng[16], D. Notz, K. Ohrenberg[14], I.H. Park[17], A. Pellegrino, F. Pelucchi, K. Piotrzkowski, M. Roco[18], M. Rohde, J. Roldán, A.A. Savin, U. Schneekloth, W. Schulz[19], F. Selonke, B. Surrow, E. Tassi, T. Voß[20], D. Westphal, G. Wolf, U. Wollmer, C. Youngman, A.F. Żarnecki, W. Zeuner
Deutsches Elektronen-Synchrotron DESY, Hamburg, Germany

B.D. Burow, H.J. Grabosch, A. Meyer, S. Schlenstedt
DESY-IfH Zeuthen, Zeuthen, Germany

G. Barbagli, E. Gallo, P. Pelfer
University and INFN, Florence, Italy [f]

G. Maccarrone, L. Votano
INFN, Laboratori Nazionali di Frascati, Frascati, Italy [f]

A. Bamberger, S. Eisenhardt, P. Markun, T. Trefzger[21], S. Wölfle
Fakultät für Physik der Universität Freiburg i.Br., Freiburg i.Br., Germany [c]

J.T. Bromley, N.H. Brook, P.J. Bussey, A.T. Doyle, D.H. Saxon, L.E. Sinclair, E. Strickland, M.L. Utley[22], R. Waugh, A.S. Wilson
Dept. of Physics and Astronomy, University of Glasgow, Glasgow, U.K. [o]

I. Bohnet, N. Gendner, U. Holm, A. Meyer-Larsen, H. Salehi, K. Wick
Hamburg University, I. Institute of Exp. Physics, Hamburg, Germany [c]

L.K. Gladilin[23], R. Klanner, E. Lohrmann, G. Poelz, W. Schott[24], F. Zetsche
Hamburg University, II. Institute of Exp. Physics, Hamburg, Germany [c]

T.C. Bacon, I. Butterworth, J.E. Cole, V.L. Harris, G. Howell, B.H.Y. Hung, L. Lamberti[25], K.R. Long, D.B. Miller, N. Pavel, A. Prinias[26], J.K. Sedgbeer, D. Sideris, A.F. Whitfield[27]
Imperial College London, High Energy Nuclear Physics Group, London, U.K. [o]

U. Mallik, S.M. Wang, J.T. Wu
University of Iowa, Physics and Astronomy Dept., Iowa City, USA [p]

P. Cloth, D. Filges
Forschungszentrum Jülich, Institut für Kernphysik, Jülich, Germany

S.H. An, S.B. Lee, S.W. Nam, H.S. Park, S.K. Park
Korea University, Seoul, Korea [h]

F. Barreiro, J.P. Fernandez, R. Graciani, J.M. Hernández, L. Hervás, L. Labarga, M. Martinez, J. del Peso, J. Puga, J. Terron, J.F. de Trocóniz
Univer. Autónoma Madrid, Depto de Física Teóríca, Madrid, Spain [n]

F. Corriveau, D.S. Hanna, J. Hartmann, L.W. Hung, J.N. Lim, W.N. Murray, A. Ochs, M. Riveline, D.G. Stairs, M. St-Laurent, R. Ullmann
McGill University, Dept. of Physics, Montréal, Québec, Canada [a], [b]

T. Tsurugai
Meiji Gakuin University, Faculty of General Education, Yokohama, Japan

V. Bashkirov, B.A. Dolgoshein, A. Stifutkin
Moscow Engineering Physics Institute, Mosocw, Russia [l]

G.L. Bashindzhagyan, P.F. Ermolov, Yu.A. Golubkov, V.D. Kobrin, I.A. Korzhavina, V.A. Kuzmin, O.Yu. Lukina, A.S. Proskuryakov, L.M. Shcheglova, A.N. Solomin, N.P. Zotov
Moscow State University, Institute of Nuclear Physics, Moscow, Russia [m]

C. Bokel, M. Botje, N. Brümmer, F. Chlebana[18], J. Engelen, M. de Kamps, P. Kooijman, A. Kruse, A. van Sighem, H. Tiecke, W. Verkerke, J. Vossebeld, M. Vreeswijk, L. Wiggers, E. de Wolf
NIKHEF and University of Amsterdam, Netherlands [i]

D. Acosta, B. Bylsma, L.S. Durkin, J. Gilmore, C.M. Ginsburg, C.L. Kim, T.Y. Ling, P. Nylander, T.A. Romanowski[28]
Ohio State University, Physics Department, Columbus, Ohio, USA [p]

H.E. Blaikley, R.J. Cashmore, A.M. Cooper-Sarkar, R.C.E. Devenish, J.K. Edmonds, N. Harnew, M. Lancaster[29], J.D. McFall, C. Nath, V.A. Noyes[26], A. Quadt, J.R. Tickner, H. Uijterwaal, R. Walczak, D.S. Waters, T. Yip
Department of Physics, University of Oxford, Oxford, U.K. [o]

A. Bertolin, R. Brugnera, R. Carlin, F. Dal Corso, U. Dosselli, S. Limentani, M. Morandin, M. Posocco, L. Stanco, R. Stroili, C. Voci
Dipartimento di Fisica dell' Universita and INFN, Padova, Italy [f]

J. Bulmahn, R.G. Feild[30], B.Y. Oh, J.R. Okrasiński, J.J. Whitmore
Pennsylvania State University, Dept. of Physics, University Park, PA, USA [q]

G. Marini, A. Nigro
Dipartimento di Fisica, Univ. 'La Sapienza' and INFN, Rome, Italy [f]

J.C. Hart, N.A. McCubbin, T.P. Shah
Rutherford Appleton Laboratory, Chilton, Didcot, Oxon, U.K. [o]

E. Barberis[29], T. Dubbs, C. Heusch, M. Van Hook, W. Lockman, J.T. Rahn, H.F.-W. Sadrozinski, A. Seiden, D.C. Williams
University of California, Santa Cruz, CA, USA [p]

O. Schwarzer, A.H. Walenta
Fachbereich Physik der Universität-Gesamthochschule Siegen, Germany [c]

H. Abramowicz, G. Briskin, S. Dagan[31], T. Doeker, S. Kananov, A. Levy[32]
Raymond and Beverly Sackler Faculty of Exact Sciences, School of Physics, Tel-Aviv University, Tel-Aviv, Israel [e]

T. Abe, J.I. Fleck[33], M. Inuzuka, T. Ishii, M. Kuze, K. Nagano, M. Nakao, I. Suzuki, K. Tokushuku, K. Umemori, S. Yamada, Y. Yamazaki
Institute for Nuclear Study, University of Tokyo, Tokyo, Japan [g]

R. Hamatsu, T. Hirose, K. Homma, S. Kitamura[34], T. Matsushita, K. Yamauchi
Tokyo Metropolitan University, Dept. of Physics, Tokyo, Japan [g]

R. Cirio, M. Costa, M.I. Ferrero, S. Maselli, V. Monaco, C. Peroni, M.C. Petrucci, R. Sacchi, A. Solano, A. Staiano
Universita di Torino, Dipartimento di Fisica Sperimentale and INFN, Torino, Italy [f]

M. Dardo
II Faculty of Sciences, Torino University and INFN - Alessandria, Italy [f]

D.C. Bailey, M. Brkic, C.-P. Fagerstroem, G.F. Hartner, K.K. Joo, G.M. Levman, J.F. Martin, R.S. Orr, S. Polenz, C.R. Sampson, D. Simmons, R.J. Teuscher[33]
University of Toronto, Dept. of Physics, Toronto, Ont., Canada [a]

J.M. Butterworth, C.D. Catterall, T.W. Jones, P.B. Kaziewicz, J.B. Lane, R.L. Saunders, J. Shulman, M.R. Sutton
University College London, Physics and Astronomy Dept., London, U.K. [o]

B. Lu, L.W. Mo
Virginia Polytechnic Inst. and State University, Physics Dept., Blacksburg, VA, USA [q]

J. Ciborowski, G. Grzelak[35], M. Kasprzak, K. Muchorowski[36], R.J. Nowak, J.M. Pawlak, R. Pawlak, T. Tymieniecka, A.K. Wróblewski, J.A. Zakrzewski
Warsaw University, Institute of Experimental Physics, Warsaw, Poland [j]

M. Adamus
Institute for Nuclear Studies, Warsaw, Poland [j]

C. Coldewey, Y. Eisenberg[31], D. Hochman, U. Karshon[31], D. Revel[31]
Weizmann Institute, Nuclear Physics Dept., Rehovot, Israel [d]

W.F. Badgett, D. Chapin, R. Cross, S. Dasu, C. Foudas, R.J. Loveless, S. Mattingly, D.D. Reeder, W.H. Smith, A. Vaiciulis, M. Wodarczyk
University of Wisconsin, Dept. of Physics, Madison, WI, USA [p]

S. Bhadra, W.R. Frisken, M. Khakzad, W.B. Schmidke
York University, Dept. of Physics, North York, Ont., Canada [a]

[1] also at IROE Florence, Italy
[2] now at Univ. of Salerno and INFN Napoli, Italy
[3] now at Univ. of Crete, Greece
[4] supported by Worldlab, Lausanne, Switzerland
[5] now OPAL
[6] retired
[7] also at University of Torino and Alexander von Humboldt Fellow
[8] now at Dongshin University, Naju, Korea
[9] also at DESY and Alexander von Humboldt Fellow
[10] Alfred P. Sloan Foundation Fellow
[11] supported by an EC fellowship number ERBFMBICT 950172
[12] visitor from Florida State University
[13] now at ALCATEL Mobile Communication GmbH, Stuttgart
[14] now at DESY Computer Center
[15] supported by European Community Program PRAXIS XXI
[16] now at DESY-Group FDET
[17] visitor from Kyungpook National University, Taegu, Korea, partially supported by DESY
[18] now at Fermi National Accelerator Laboratory (FNAL), Batavia, IL, USA
[19] now at Siemens A.G., Munich
[20] now at NORCOM Infosystems, Hamburg
[21] now at ATLAS Collaboration, Univ. of Munich
[22] now at Clinical Operational Research Unit, University College, London
[23] on leave from MSU, supported by the GIF, contract I-0444-176.07/95
[24] now a self-employed consultant
[25] supported by an EC fellowship
[26] PPARC Post-doctoral Fellow
[27] now at Conduit Communications Ltd., London, U.K.
[28] now at Department of Energy, Washington
[29] now at Lawrence Berkeley Laboratory, Berkeley
[30] now at Yale University, New Haven, CT
[31] supported by a MINERVA Fellowship
[32] partially supported by DESY
[33] now at CERN
[34] present address: Tokyo Metropolitan College of Allied Medical Sciences, Tokyo 116, Japan
[35] supported by the Polish State Committee for Scientific Research, grant No. 2P03B09308
[36] supported by the Polish State Committee for Scientific Research, grant No. 2P03B09208

[a] supported by the Natural Sciences and Engineering Research Council of Canada (NSERC)
[b] supported by the FCAR of Québec, Canada
[c] supported by the German Federal Ministry for Education and Science, Research and Technology (BMBF), under contract numbers 057BN19P, 057FR19P, 057HH19P, 057HH29P, 057SI75I
[d] supported by the MINERVA Gesellschaft für Forschung GmbH, the German Israeli Foundation, and the U.S.-Israel Binational Science Foundation
[e] supported by the German Israeli Foundation, and by the Israel Science Foundation
[f] supported by the Italian National Institute for Nuclear Physics (INFN)
[g] supported by the Japanese Ministry of Education, Science and Culture (the Monbusho) and its grants for Scientific Research
[h] supported by the Korean Ministry of Education and Korea Science and Engineering Foundation
[i] supported by the Netherlands Foundation for Research on Matter (FOM)
[j] supported by the Polish State Committee for Scientific Research, grant No. 115/E-343/SPUB/P03/120/96
[k] supported by the Polish State Committee for Scientific Research (grant No. 2 P03B 083 08) and Foundation for Polish-German Collaboration
[l] partially supported by the German Federal Ministry for Education and Science, Research and Technology (BMBF)
[m] supported by the German Federal Ministry for Education and Science, Research and Technology (BMBF), and the Fund of Fundamental Research of Russian Ministry of Science and Education and by INTAS-Grant No. 93-63
[n] supported by the Spanish Ministry of Education and Science through funds provided by CICYT
[o] supported by the Particle Physics and Astronomy Research Council
[p] supported by the US Department of Energy
[q] supported by the US National Science Foundation

1 Introduction

Deep–inelastic scattering (DIS) of leptons on nucleons has been an important tool for understanding nucleon structure and many elements of the Standard Model, including both the electroweak interaction and quantum chromodynamics (QCD). At the HERA collider, DIS processes are being studied at a center of mass energy $\sqrt{s} = 300\,\mathrm{GeV}$ and at Q^2 (the negative of the square of the four-momentum transfer) exceeding the squares of the weak vector boson masses. In this regime, lepton–nucleon scattering allows unique and sensitive tests of the Standard Model as well as of certain extensions to it [1].

This paper presents results from e^+p running with the ZEUS detector during the years 1994 to 1996, at proton and positron beam energies of $E_p = 820\,\mathrm{GeV}$ and $E_e = 27.5\,\mathrm{GeV}$. With the integrated luminosity of $20.1\,\mathrm{pb}^{-1}$ collected in this period, it has become possible to study the reaction $e^+p \to e^+X$ in the region where the expected DIS cross section is in the subpicobarn range. This region of high Q^2 and x (the Bjorken scaling variable) has never before been explored. The above reaction is understood to be a positron–quark collision with center–of–mass energy $\sqrt{xs}$. Initial cross section measurements by the ZEUS [2] and H1 [3] collaborations are in good agreement with Standard Model expectations for Q^2 up to about $10^4\,\mathrm{GeV}^2$. In this paper, we report on a more sensitive search for deviations from Standard Model predictions in the region $Q^2 > 5000\,\mathrm{GeV}^2$.

2 Neutral Current Deep–Inelastic Scattering

The reaction studied is:

$$e^+ + p \to e^+ + X \tag{1}$$

where X represents the final state hadronic system. In the high Q^2 regime, the Standard Model neutral current (NC) cross section for (1) depends on well–measured electroweak parameters and on the parton densities in the proton. Though the latter have not yet been measured at high Q^2, perturbative Quantum Chromodynamics (pQCD) predicts their values through evolution from high–precision measurements made at lower Q^2 values.

The Born cross section [4] for the NC DIS reaction (1) with unpolarized beams is[1]

$$\frac{d^2\sigma}{dx\,dQ^2} = \frac{2\pi\alpha^2}{xQ^4}\left\{Y_+(y)\,\mathcal{F}_2(x,Q^2) - Y_-(y)\,x\mathcal{F}_3(x,Q^2)\right\}\,, \tag{2}$$

where α is the electromagnetic coupling. The cross section is given in terms of Q^2 and the DIS scaling variables x and $y = Q^2/sx$. In the region of large x and Q^2 studied here, the parity–violating $x\mathcal{F}_3$ term substantially reduces the e^+p cross section, while increasing the cross section for e^-p scattering (where the second term has positive sign). The explicit y–dependence, which is due to the helicity dependence of electroweak interactions, is contained in the functions

$$Y_\pm(y) = 1 \pm (1-y)^2\,, \tag{3}$$

[1] We neglect the contribution to the cross section (2) of the longitudinal structure function, $\mathcal{F}_L$, which we estimate from pQCD and the parton densities[5] to be less than 1% in the kinematic range under study.

while the dependence on the quark structure of the proton, and on the Z^0 propagator is absorbed in the (positive) structure functions:

$$\left(\begin{array}{c} \mathcal{F}_2(x,Q^2) \\ x\mathcal{F}_3(x,Q^2) \end{array} \right) = x \sum_{q=\text{quarks}} \left(\begin{array}{c} C_2^q(Q^2)[q(x,Q^2)+\overline{q}(x,Q^2)] \\ C_3^q(Q^2)[q(x,Q^2)-\overline{q}(x,Q^2)] \end{array} \right) \tag{4}$$

written in terms of the quark densities in the proton ($q = u,\ d,\ c,\ s,\ t,\ b$) and the corresponding antiquark densities $\overline{q}$. For e^+p scattering, the Q^2–dependent coefficient functions, C_2^q and C_3^q, are given by:

$$\begin{array}{lll} C_2^q(Q^2) = & e_q^2 & -2e_q v_q v_e \chi_Z + (v_q^2+a_q^2)(v_e^2+a_e^2)\chi_Z^2 \\ C_3^q(Q^2) = & & -2e_q a_q a_e \chi_Z + (2v_q a_q)(2v_e a_e)\chi_Z^2 \end{array} \tag{5}$$

with

$$\chi_Z = \frac{1}{4\sin^2\theta_w \cos^2\theta_w} \frac{Q^2}{Q^2+M_Z^2}\ . \tag{6}$$

In eqs. 5 and 6, M_Z is the Z^0 mass, e_q is the quark charge in units of the positron charge, $v_q = (T_{3q} - 2e_q \sin^2\theta_w)$ and $a_q = T_{3q}$ are the vector and axial vector couplings of the quark to the Z^0, v_e and a_e are the corresponding electron couplings, θ_w is the weak mixing angle, and T_3 is the third component of the weak isospin. All relevant electroweak parameters have been measured to high precision [6].

The QCD–evolved structure functions [7] of equation (4), evaluated at a given x at high Q^2, depend on quark and gluon densities in the proton measured at lower values of Q^2 and higher values of x. At high x, u quarks give the dominant contribution to the cross section because they have the largest density [8] and because $e_u = 2/3$. In addition, the antiquark ($\overline{q}$) density is small [9].

Uncertainties in the Born-level e^+p DIS cross section predictions in this region of high x and Q^2 are estimated to be about 6.5% (see Section 8), mainly due to uncertainties in the evolved quark densities.

It should be noted that an anomalously high cross section for the production of jets with high transverse energy in $p\overline{p}$ collisions, as recently reported by the CDF collaboration [10], can be explained by adjusting the gluon density in the proton [11] (which raises the rate of gluon–quark collisions at high x), rather than by adjusting quark densities. This variation of the gluon density, however, has only a small effect on the cross section predictions relevant to this paper (see Section 8).

3 ZEUS Detector and Monte–Carlo Simulation

3.1 Experimental Setup

A description of the ZEUS detector can be found in references [12, 13]. The primary components used in this analysis were the compensating uranium–scintillator calorimeter, the central tracking detector, and the luminosity detector.

The calorimeter [14] is divided into three parts, forward (FCAL) covering the polar angle[2] interval $2.6°<\theta<37°$, barrel (BCAL: $37°<\theta<129°$) and rear (RCAL: $129°<\theta<176.1°$). The calorimeters are subdivided into towers which each subtend solid angles from 0.006 to 0.04 steradians. Each tower is longitudinally segmented into an electromagnetic (EMC) section and two hadronic (HAC) sections (one in RCAL). Each HAC section consists of a single cell, while the EMC section of each tower is further subdivided transversely into four cells (two in RCAL). In test beam conditions, for particle energies up to 120 GeV, energy resolutions of $\sigma_E/E=18\%/\sqrt{E(\mathrm{GeV})}$ for electrons and $\sigma_E/E=35\%/\sqrt{E(\mathrm{GeV})}$ for hadrons have been measured. The cell-to-cell variations in the energy calibration are approximately 2% for the EMC cells and 3% for HAC cells. The FCAL and BCAL energy scales are presently understood to an accuracy of 3%. The time resolution is below 1 ns for energy deposits greater than 4.5 GeV. The impact point of the scattered positron at the calorimeter, determined using pulse height sharing, has a resolution of about 1 cm.

In the physics analysis, only those calorimeter cells with energy deposits above thresholds of 60 MeV and 110 MeV for EMC and HAC cells respectively were used.

The central tracking chamber (CTD) [15] operates in a 1.43 T solenoidal magnetic field. It is a drift chamber consisting of 72 cylindrical layers, organized into 9 superlayers. A momentum measurement requires a track to pass through at least two superlayers, corresponding to a polar angle region of $15°<\theta<164°$. The transverse momentum resolution is $\sigma(p_t)/p_t = [0.005p_t(\mathrm{GeV})] \oplus 0.016$ for full length tracks. For full length tracks with momenta $p > 5$ GeV the vertex resolution is 0.1 cm in the transverse plane and 0.4 cm along Z.

Events were filtered online by a three–level trigger system [13]. The trigger criteria used in this analysis relied primarily on the energies measured in the calorimeter. The first level trigger decision was based on electromagnetic energy and total transverse energy (E_t). The second level trigger rejected backgrounds (mostly p–gas interactions) for which the calorimeter timing was inconsistent with an ep interaction. In addition, the second level trigger applied increased E_t thresholds and also required a minimum value of $E - p_Z$ (see Section 5), where E and p_Z are the summed energy and Z-component of the momentum measured in the calorimeter. The third level trigger applied more stringent timing cuts as well as increased energy and $E - p_Z$ thresholds. In all cases, the requirements were less stringent than those imposed by the offline event selection.

The luminosity was measured by the rate of high energy photons from the process $ep \to ep\gamma$ detected in a lead–scintillator calorimeter [16] located at $Z = -107$ m. The uncertainty associated with luminosity measurements is addressed in section 8.

3.2 Monte Carlo Simulation

NC DIS events were simulated using the MEPS option of LEPTO [17] interfaced to HERACLES [18] via DJANGO [19] and the MRSA parton distribution set [20]. The event simulation included electroweak radiative corrections, leading order QCD effects and parton showers. Hadronization was simulated with JETSET[21].

[2]The right-handed ZEUS coordinate system is centered on the nominal interaction point ($Z = 0$) and defined with the Z axis pointing in the proton beam direction, and the horizontal X axis pointing towards the center of HERA.

Large samples of simulated photoproduction events[22] were used for background studies. Samples of both direct and resolved photoproduction events (including the production of $c\overline{c}$ and $b\overline{b}$ pairs) were generated using both PYTHIA [21] and HERWIG [23]. Direct and resolved photoproduction of events with prompt photons were simulated with HERWIG. Production of W and Z bosons was studied using the EPVEC [24] generator. Finally, the processes $\gamma\gamma \to e^+e^-$ and $\gamma\gamma \to \tau^+\tau^-$ were simulated using ZLPAIR [25].

All MC events were passed through a GEANT [26] based simulation of the ZEUS detector and trigger, and analyzed with the same reconstruction and offline selection procedures as the data.

4 Positron Identification and Event Kinematics

A key signature of high Q^2 $e^+p \to e^+X$ events is an isolated high transverse momentum positron. In order to identify and reconstruct this positron, while rejecting events in which other final state particles mimic a positron, an algorithm was used which combines calorimeter and CTD information.

In a first step, the calorimeter cells are clustered by joining each cell to the highest energy cell among its adjacent neighbours. All clusters are evaluated as positron candidates. The cluster energy, $E_{\rm clu}$, is the sum of the cell energies belonging to the cluster. The cluster angle, $\theta_{\rm clu}$, is set equal to the polar angle obtained by joining the energy-weighted mean position of the cluster with the event vertex obtained from the tracks measured with the CTD. For candidates with polar angle[3] within the CTD acceptance ($\theta_{\rm clu} > 17.2^\circ$), a matching track is required. A track is considered to match if the distance of closest approach (DCA) between the extrapolation of the track into the calorimeter and the position of the cluster center is less than 10 cm, where the r. m. s. resolution on the DCA is 1.8 cm.

In the second step, several quantities, ξ_i, are calculated for each positron candidate: the fraction of the cluster energy in the HAC sections of the calorimeter, the parameters related to lateral energy profiles, and the total energy ($E_{\rm cone}$) in all calorimeter cells not associated with the cluster but lying within an η, ϕ (pseudorapidity,azimuth) cone of radius 0.8 centered on the cluster. If a matching track is present, we also evaluate the polar and azimuthal angle differences between the track and the cluster position, and the quantity $1/E_{\rm clu} - 1/P_{\rm trk}$, where $P_{\rm trk}$ is the track momentum.

Finally, we transform each ξ_i into a quality factor $Q(\xi_i)$. Candidates are accepted as positrons if the product of the $Q(\xi_i)$ exceeds a threshold determined from Monte Carlo studies. The efficiency for finding positrons in a neutral current DIS sample with $Q^2 > 5000\,{\rm GeV}^2$ is 91%. In accepted events, the positron energy, E'_e, is set equal to the cluster energy, $E_{\rm clu}$, and the positron angle, θ_e, is set equal to $\theta_{\rm clu}$. The resolution in θ_e is typically better than 0.3°.

For each event with an accepted positron, the following global event quantities were

[3]We do not consider candidates with $\theta_{\rm clu} > 164^\circ$ (which are also beyond the CTD acceptance limit), since they correspond to Q^2 values below the range of this analysis.

calculated from the energy deposits in the calorimeter:

$$\begin{aligned} p_t &= \sqrt{\left(\sum_i p_X^i\right)^2 + \left(\sum_i p_Y^i\right)^2}\,, \\ E - p_Z &= \sum_i \left(E^i - p_Z^i\right)\,, \\ E_t &= \sum_i \sqrt{(p_X^i)^2 + (p_Y^i)^2}\,, \\ (p_t)_{\rm had} &= \sqrt{\left(\sum_i{}' p_X^i\right)^2 + \left(\sum_i{}' p_Y^i\right)^2}\,, \\ (E - p_Z)_{\rm had} &= \sum_i{}' \left(E^i - p_Z^i\right)\,, \end{aligned} \tag{7}$$

where the sums run over all calorimeter cells with energy deposits above threshold and the $\vec{p}^{\,i}$ are the momenta assigned to each calorimeter cell (calculated assuming zero mass with the direction obtained from the cell center and the measured vertex position). The primed sums exclude the cells associated with the positron.

To describe the hadronic system, we use the angle, $\gamma_{\rm raw}$, and energy, E_q, defined as

$$\cos\gamma_{\rm raw} = \frac{(p_t)^2_{\rm had} - (E-p_Z)^2_{\rm had}}{(p_t)^2_{\rm had} + (E-p_Z)^2_{\rm had}} \qquad \text{and} \qquad E_q = \frac{(p_t)_{\rm had}}{\sin\gamma_{\rm raw}}\,. \tag{8}$$

Resolution effects and systematic shifts of $\gamma_{\rm raw}$ have been studied with MC simulations. The reconstructed $\gamma_{\rm raw}$ is systematically higher than the generated value by about 2.7°. To remove this bias, we compute a corrected value, γ, which depends on $\gamma_{\rm raw}$ and θ_e. The r. m. s. resolution of γ is about 2.5° for $x > 0.55$ and $Q^2 > 5000\,{\rm GeV}^2$.

In the quark–parton model, for a perfect detector, γ and E_q are interpreted as the scattering angle and energy of the massless quark q in the reaction $eq \to eq$.

At a given value of s, the kinematic variables (x, y, and Q^2) can be reconstructed from any two of the four measured quantities: E'_e, θ_e, E_q, and γ. Different combinations have been used by the HERA experiments. At high x and Q^2 where the calorimeter energy resolution functions are narrow, the dominant uncertainties in energy measurements are due to systematic effects such as energy loss in inactive material in front of the calorimeter, nonuniformities and nonlinearities in the calorimeter response, longitudinal energy leakages, and energy carried away by neutrinos and muons. For the hadronic system, the raw measured energies are typically 15% less than the true energies. For positrons, the raw measured energies are typically 4% less than the true values.

We choose the double–angle method [27] because it is least sensitive to uncertainties in the energy measurement. In this scheme, the kinematic variables are obtained from θ_e and γ as follows:

$$\begin{aligned} x_{\rm DA} &= \frac{E_e}{E_p}\,\frac{\sin\gamma}{(1-\cos\gamma)}\,\frac{\sin\theta_e}{(1-\cos\theta_e)}\,, \\ y_{\rm DA} &= \frac{\sin\theta_e(1-\cos\gamma)}{\sin\gamma + \sin\theta_e - \sin(\gamma+\theta_e)}\,, \\ Q^2_{\rm DA} &= s\; x_{\rm DA}\; y_{\rm DA}\,. \end{aligned} \tag{9}$$

For $y > 0.25$ and $x > 0.45$, the resolution in $x_{\rm DA}$ is 9%; it improves to 6% for $y > 0.5$. The resolution in $Q^2_{\rm DA}$ is typically 5% at large x and y.

For selected events with high x and high Q^2 we also present the kinematic variables calculated from the scattered positron energy E'_e and angle θ_e using the equations:

$$\begin{aligned} x_e &= \frac{E_e}{E_p}\,\frac{E'_e(1+\cos\theta_e)}{2E_e - E'_e(1-\cos\theta_e)}\,, \\ y_e &= 1 - \frac{E'_e}{2E_e}(1-\cos\theta_e)\,, \\ Q^2_e &= s\; x_e\; y_e\,. \end{aligned} \tag{10}$$

We apply a test–beam based correction to E'_e to account for energy loss in inactive material and nonuniformities of the calorimeter response.

5 Event Selection

Important characteristics of reaction (1) that distinguish it from background processes include (i) the presence of an energetic isolated positron, (ii) p_t balance, and (iii) $E - p_Z \approx 2E_e = 55\,\text{GeV}$. In addition, at large Q^2, the transverse energy E_t typically exceeds 100 GeV.

About 10^6 events were accepted by the trigger requirements described in section 3.1. The offline event selection criteria are described below.

- $E - p_Z$
  The net $E - p_Z$ as measured in the calorimeter is required to be in the range $40\,\text{GeV} < E - p_Z < 70\,\text{GeV}$ ($44\,\text{GeV} < E - p_Z < 70\,\text{GeV}$) for $\theta_e > 17.2°$ ($\theta_e < 17.2°$). The lower cut rejects backgrounds such as photoproduction or $e^+p \to e^+X$ events with a hard initial state photon, for which energy escapes through the rear beam hole (see below). The 70 GeV cut removes a small number of events with a misreconstructed vertex position.

- Longitudinal vertex position
  The event vertex reconstructed from CTD tracks must have a Z position ($Z_{\rm vtx}$) within 50 cm of the nominal interaction point. The $Z_{\rm vtx}$ distribution of the data is roughly Gaussian with $\langle Z_{\rm vtx}\rangle = -2\,\text{cm}$. The r. m. s. spread in $Z_{\rm vtx}$, 12 cm, is largely due to the length of the proton beam bunches.

- Positron requirements
  An isolated positron candidate with energy $E'_e > 20\,\text{GeV}$ and $E_{\rm cone} < 5\,\text{GeV}$ must be found by the algorithm described in section 4. Additional requirements depend on the polar angle of the positron:

  For $\theta_e > 17.2°$, where the positron candidates are within the CTD acceptance, a matching track with momentum above 2 GeV is required.

For $\theta_e < 17.2°$, where the positron either misses the CTD altogether or is on the edge of the CTD acceptance, the number of fake positron candidates is large. These have a sharply falling transverse momentum spectrum. To reduce this background, we require positron candidates in this angular range to have transverse momenta above 30 GeV.

To remove Compton scattering events ($ep \to e\gamma X$), we reject any event which has two isolated electromagnetic clusters in the calorimeter, each with $E_{\rm clu} > 8\,\text{GeV}$ and $E_{\rm cone} < 2\,\text{GeV}$.

- Momentum transfer
  We require $Q^2_{\rm DA}$ to exceed $5000\,\text{GeV}^2$.

The overall selection efficiency, estimated using Monte Carlo NC events generated with $Q^2 > 5000\,\text{GeV}^2$, is 81%. For the 191 events which pass all cuts, the mean measured $E - p_Z$ is 51.9 GeV with an r. m. s. width of 4.2 GeV, in good agreement with the Monte Carlo e^+p NC simulation which predicts a mean of 51.8 GeV and an r. m. s. of 4.0 GeV. While no cut was applied to the net transverse momentum (p_t), the surviving events have a mean p_t of 7.5 GeV, again in good agreement with the e^+p NC Monte Carlo prediction of 7.1 GeV.

6 Data and Expectations at Large x and Q^2

Figure 1 shows the distribution in the $(x_{\rm DA}, y_{\rm DA})$ plane of the 191 events satisfying the selection criteria. In Table 1, the numbers of observed events are compared with the Standard Model expectations in bins of $x_{\rm DA}$ and $y_{\rm DA}$. In general, the agreement between the data and the Standard Model expectations is good. However, five events, in four $(x_{\rm DA}, y_{\rm DA})$ bins occur at high $x_{\rm DA}$ and $Q^2_{\rm DA}$ where the expected numbers of events are small. Four lie in the region $x_{\rm DA} > 0.55$ and $y_{\rm DA} > 0.25$, while the fifth has $x_{\rm DA} = 0.48$ and a very high $Q^2_{\rm DA}$. These five events are selected for more detailed discussion below.

Figures 2 and 3 show the $x_{\rm DA}$ (for $y_{\rm DA} > 0.25$) and $Q^2_{\rm DA}$ distributions of the final event sample. In both figures, the e^+p NC prediction for the same integrated luminosity is superimposed as a solid histogram. Again, the agreement with the Standard Model is good at lower values of $x_{\rm DA}$ and $Q^2_{\rm DA}$, but an excess is observed at high $x_{\rm DA}$ and at high $Q^2_{\rm DA}$.

Table 2 shows the kinematic variables, before applying the corrections discussed in section 4, associated with the five selected events. Included are the uncorrected values of $x_{\rm DA}$, $y_{\rm DA}$, and $Q^2_{\rm DA}$ (calculated using $\gamma_{\rm raw}$) as well as the corrected value of γ. Table 3 gives the kinematic variables and their estimated uncertainties obtained using the double–angle and electron methods. The uncertainties have been estimated from the resolutions in γ and θ_e, as well as estimates of the systematic uncertainty in the γ–correction procedure discussed in Section 4. The quoted r. m. s. errors on the electron variables include the uncertainty in θ_e, the calorimeter energy resolution, the uncertainty associated with the calorimeter nonlinearity, and the uncertainty on corrections applied for inactive material and nonuniformities. Though θ_e is used in both the DA and electron methods, it makes

only a small contribution to each error. Hence the errors on the two measurements are essentially independent.

All events listed in Tables 2 and 3, except the first, have a track matching the electromagnetic shower of the scattered positron in the calorimeter. In these events, the positron track momentum is consistent with the calorimeter energy within measurement errors[4]. The first event (11-Oct-94) has a positron candidate at too small an angle to produce an observable track in the CTD.[5] We show event displays of the first two events in Figs. 4 and 5.

The five events have clean, well-identified and isolated positrons and jets in the final state. None lie close to any of the selection cuts described in the previous section. For these events, the scattering angles and energies of the final state positrons and jets are measured with good precision, making it unlikely that resolution smearing has moved any of these events from low Q^2 to the measured Q^2_{DA}.

Initial state radiation (ISR) from the incoming positron, where the radiated photon escapes through the rear beam hole is a possible source of uncertainty in the determination of the event kinematics. Since ISR affects the DA and electron variables differently, it is possible to estimate the energy E_γ of the radiated photon. For each of the five events, E_γ is consistent with zero within resolution and the measured values of $E - p_Z$ limit $E_\gamma \lesssim 3\,\mathrm{GeV}$.

7 Background Estimation

Potential backgrounds to e^+p DIS events at large x and y are those processes which yield an isolated positron or electron of high transverse energy, or a photon or π^0 which could be misidentified as a scattered positron. The latter event class contributes predominantly to the background of events in which the positron is very forward ($\theta_e \lesssim 17.2^\circ$) and no track information is available for the positron candidate (e.g. the first event in Tables 2 and 3). At larger angles, photon conversions in inactive material between the interaction point and the CTD can also mimic positron candidates with matching tracks, but this effect, which is included in the detector simulation, is much smaller.

In the following, we describe the physical processes studied as possible sources of background. Limits are quoted at 90% confidence level.

- Prompt photon photoproduction ($\gamma p \to \gamma X$) has been studied using HERWIG. We generated an event sample with the final state photon transverse momentum exceeding 20 GeV. The cross section is 1.6 pb, of which 86% (14%) is due to direct (resolved) photoproduction. The observed cross section due to this process in the region $x_{\mathrm{DA}} > 0.45$ and $y_{\mathrm{DA}} > 0.25$ is 0.28 fb (0.006 events).

- Photoproduction of high E_t jets can contribute to the background if a jet is misidentified as a positron. Using HERWIG, we have generated event samples for both direct

[4] It should be noted that the positron energies in table 2 are so large that the tracking error does not allow an unambiguous determination of the particle charge.

[5] There are hits in the innermost layer of the CTD, aligned in azimuth with this positron candidate. However, the hits are too few to qualify as a track according to our standard criteria.

and resolved processes which include heavy quark production and decay. In these samples, no event satisfies the selection criteria for $x_{\rm DA} > 0.45$ and $y_{\rm DA} > 0.25$, providing an upper limit of 1.8 fb (0.04 events).

- QED Compton scattering ($ep \to e\gamma X$) could produce background if one of the electromagnetic showers is not recognized as such. Monte Carlo studies show that this probability is negligible, with an upper limit on the contribution to the observed cross section of 0.2 fb (0.004 events).

- Two photon production of lepton pairs ($\gamma\gamma \to \ell\ell$) was studied using ZLPAIR. No events from the process $\gamma\gamma \to e^+e^-$ were found after the selections. For $\gamma\gamma \to \tau^+\tau^-$, where one τ decays via $\tau \to e\nu$, the quantity $E-p_Z$ as well as the electron transverse energy are typically much lower than for high Q^2 NC events. We obtain the upper limit on the contribution to the observed cross section of 0.1 fb (0.002 events).

- Leptonic decays of W bosons have been studied using a Monte Carlo sample generated with EPVEC. The total cross section for production of $W^{\pm}$ bosons and their subsequent decay via $W \to e\nu_e$ is approximately 0.1 pb. The final state contains a (anti)neutrino with high transverse momentum (of order 40 GeV), which typically results in large missing $E - p_Z$ (as well as p_t). We estimate the accepted cross section for this process to be less than 0.5 fb (0.01 events). Decays of the neutral boson, $Z^0 \to e^+e^-$, are rejected by the cut on two electromagnetic clusters and are expected to contribute a negligible background.

The estimated cross sections from these background sources are listed in Table 4 along with the e^+p NC cross section. The backgrounds are much smaller than the DIS signal in the region of interest, and are neglected.

8 Uncertainties of the Standard Model Predictions

The predicted numbers of e^+p NC DIS events depend on (i) the measured luminosity, (ii) the electroweak parameters, (iii) electroweak radiative corrections, mainly due to initial state radiation (ISR), (iv) the quark densities in the relevant region of x and Q^2 and (v) the Monte Carlo simulation of the detector. We now discuss the precision to which these quantities are known and describe the studies performed to determine the uncertainties of the predictions.

- Luminosity measurement
  The luminosity is measured to a precision of about 1.5 % using the ZEUS luminosity monitor. The recent 1996 running period has a larger uncertainty due to effects from beam satellite bunches. Also, the offline calibration of the luminosity detector is not yet finalized. Including these uncertainties from recent data, the uncertainty for the full data sample is 2.3%.

- Electroweak parameters
  The relevant electroweak parameters have been measured to high accuracy [6] and

contribute a small uncertainty in the predicted cross section over the HERA kinematic range [28]. The HERACLES program calculates NC DIS cross sections to first order using input values for the Fermi constant G_μ, M_Z, the top mass m_t, and the Higgs mass. Varying $M_Z = 91.187 \pm 0.007\,\text{GeV}$ and $m_t = 180 \pm 12\,\text{GeV}$ within their experimental errors [6] changes the predicted cross section in the kinematic range reported in this paper by only 0.25%.

- Radiative corrections

  The program HECTOR [29], which includes the effects of second order QED radiative corrections was used to check the cross sections computed using HERACLES. The differences were found to be about 1.5% for the integrated cross sections in the region $x_{DA} > 0.5$ and $y_{DA} > 0.25$.

  The luminosity monitor records data for all triggered events, and so measures directly, with an acceptance of about 30%, the ISR spectrum for accepted events. The experimental data are in quantitative agreement with the ISR spectrum calculated for the accepted sample.

  Corrections due to initial state radiation convoluted with the experimental resolution, based on studies [30] made for lower values of x, produce uncertainties of less than 2% in the accepted cross sections. This number is used as the estimate of the uncertainty due to radiative corrections.

- Structure functions

  The least well known inputs to the predicted cross section in equation 2 are the structure functions. To estimate the uncertainty associated with parton densities, we performed a NLO QCD fit to fixed-target F_2 lepton-proton data (with $x > 0.1$) from the NMC [31], SLAC [32], and BCDMS [33] collaborations and xF_3 and $\bar{q}/xF_3$ results from the CCFR collaboration [9]. A complete treatment of statistical and correlated experimental systematic errors was included in the fit. The results of the fit are consistent with the MRSA [20] and CTEQ3 [34] parton density parameterizations up to Q^2 of $5 \times 10^4 \text{GeV}^2$.

  The fit was used to estimate the two largest uncertainties due to the structure functions: the experimental uncertainties and the uncertainty of the quark-gluon coupling, α_s, used in the evolution to higher Q^2. The effects of experimental uncertainties in the fixed-target data result in a $\pm 6.2\%$ uncertainty in the integrated cross section at HERA for $x > 0.5$ and $y > 0.25$. The uncertainty due to α_s was estimated by varying the value of $\alpha_s(M_Z)$ used in the QCD evolution from 0.113 to 0.123, which produces an uncertainty of $\pm 1.9\%$. From the above studies, we take the overall uncertainty in the cross section due to structure function uncertainties to be $\pm 6.5\%$ over the kinematic range of interest.

  Other sources of uncertainty in the structure functions were found to be small. Changing the strange quark fraction in the QCD fit from 10% to 30% produced less than 0.1% change in the predicted cross section. Removing BCDMS data from the fit produced a change of only 1.7%. Removing data with $W^2 = sy(1-x)$ between 10 and $25\,\text{GeV}^2$ had no significant effect. Since the contribution of charm to the cross section for $x > 0.5$ and $y > 0.25$ is 0.5%, uncertainties in the charm quark mass and the charm evolution renormalization scale can be safely neglected.

As a cross check, the uncertainty of 6.5% was compared to the differences in cross section predicted by various parton density parameterizations. For example, a comparison of integrated cross sections predicted by the MRSA, CTEQ3, and GRV94 [35] parameterizations produces an r. m. s. of 2%. A comparison of the CTEQ4 HJ parameterization [11] (which was tuned to the CDF high E_t jet cross section [10]) with the nominal CTEQ4 parameterization produced an increase in cross section of only 1.9%, demonstrating the small effect at HERA of a larger gluon density at high x. Finally, a crude estimate of the contributions from QCD corrections at higher than NLO can be estimated by comparing the cross sections predicted by the GRV94 LO and NLO parameterizations, which produced a cross section difference of only 1%.

Table 5 summarizes the structure function uncertainties as well as the cross checks which were performed.

- Detector simulation
  To estimate the uncertainties in the expected event yields due to possible inaccuracies in the detector simulation, we made several modifications to the simulation to reflect uncertainties in the overall calorimeter energy scale and in the simulation of the calorimeter and CTD response to positrons. The FCAL and BCAL energy scales were separately varied by $\pm 3\%$, our present estimate of this uncertainty. Each of the seven measured quantities used in the positron identification algorithm was varied by an amount consistent with the differences between the data and the nominal simulation. For the region $x_{\rm DA} > 0.55$ and $y_{\rm DA} > 0.25$, the resulting uncertainty in the expected number of events is 4.4%.

We conclude that at the large x and Q^2 values discussed in this paper the overall uncertainty of the number of events predicted within the Standard Model is 8.4%.

9 Comparison of Data with Standard Model and Significance of Excess

Table 1 compares the data with the $e^+p \to e^+X$ expectations in bins of $x_{\rm DA}$ and $y_{\rm DA}$ for $Q^2{}_{\rm DA} > 5000\,{\rm GeV}^2$. There is very good agreement over the entire plane, except in the region of high $x_{\rm DA}$ and $y_{\rm DA}$. The numbers of observed and expected events above various $Q^2_{\rm DA}$ thresholds are given in table 6. The data agree well with the Standard Model predictions up to $Q^2_{\rm DA}$ of $1.5 \times 10^4\,{\rm GeV}^2$.

Fig. 6a shows the number of events with $Q^2_{\rm DA} > Q^{2*}_{\rm DA}$ as a function of $Q^{2*}_{\rm DA}$. Figure 7a shows the number of events with $y_{\rm DA} > 0.25$ and with $x_{\rm DA} > x^*_{\rm DA}$, as a function of $x^*_{\rm DA}$. On each of the two plots, the e^+p NC DIS Monte Carlo expectation is shown as a dotted line.

We define the Poisson probability corresponding to the event numbers in Fig. 6a as

$$\mathcal{P}\,(Q^{2*}_{\rm DA}) = \sum_{n=N_{\rm obs}}^{\infty} \frac{\mu^n}{n!} e^{-\mu} \tag{11}$$

where $N_{\rm obs}$ is the number of observed events with $Q^2_{\rm DA} > Q^{2*}_{\rm DA}$, and μ is the number of events expected from NC DIS in the same region. In Fig. 6b $\mathcal{P}(Q^{2*}_{\rm DA})$ is shown as a function of $Q^{2*}_{\rm DA}$. The minimum probability of $\mathcal{P}(Q^{2*}_{\rm DA}) = 0.39\%$ (corresponding to 2.7 Gaussian standard deviations) occurs at $Q^2_{\rm DA} = 3.75 \times 10^4\,{\rm GeV}^2$ where two events are observed while 0.091 ± 0.010 are expected. If the expected number of events is increased by its error, $\mathcal{P}(Q^{2*}_{\rm DA})$ increases to 0.47%.

We have performed a similar analysis of the $x_{\rm DA}$ spectrum in the region $y_{\rm DA} > 0.25$. The probability $\mathcal{P}(x^*_{\rm DA})$ is shown as a function of $x^*_{\rm DA}$ in Fig. 7b. Here the minimum value $\mathcal{P}(x^*_{\rm DA}) = 0.60\%$ (corresponding to 2.5 Gaussian standard deviations) occurs at $x^*_{\rm DA} = 0.57$ where four events are observed and 0.71 ± 0.06 are expected. If the expected number of events is increased by its error, $\mathcal{P}(x^*_{\rm DA})$ increases to 0.79%. The corresponding results for different $y_{\rm DA}$ cuts appear in Table 7.

To gauge the significance of these probabilities, one must consider that it is possible to observe a statistical fluctuation above *any* $Q^{2*}_{\rm DA}$ or $x^*_{\rm DA}$ within the region studied. We generated a large ensemble of simulated experiments according to Standard Model assumptions, each with a luminosity of 20.1 pb^{-1} and asked how often an experiment would have a probability $\mathcal{P}(Q^{2*}_{\rm DA}) < 0.39\%$ for *any* $Q^{2*}_{\rm DA}$. The resulting probability to find such a fluctuation was 6.0%. Similarly, we determined that the probability for an experiment to have $\mathcal{P}\,(x^*_{\rm DA}) < 0.60\%$ in the region $y_{\rm DA} > 0.25$ for *any* $x_{\rm DA}$ was 7.2%. The same analysis was applied for other $y_{\rm DA}$ cuts and the results appear in Table 7.

Finally, we have performed a statistical analysis which computes a probability for the two–dimensional distribution of the events in the $(x_{\rm DA}, y_{\rm DA})$ plane (with $Q^2_{\rm DA} > 5000\,{\rm GeV}^2$). Here the data from each simulated experiment were binned as in Table 1. Over a given region $\mathcal{R}$ of the $(x_{\rm DA}, y_{\rm DA})$ plane, which is defined as a subset of the bins shown in Table 1, we compute the likelihood for a given experiment as

$$\mathcal{L}_{\mathcal{R}} = \prod_{i \in \mathcal{R}} e^{-\mu_i} \frac{\mu_i^{N_i}}{N_i!},$$

where N_i is the number of events observed and μ_i is the number of events expected in bin i. For region $\mathcal{R}$, we denote by $\mathcal{L}^{\rm obs}_{\mathcal{R}}$ the value of $\mathcal{L}_{\mathcal{R}}$ obtained from the data.

Using the ensemble of simulated experiments, we determined the probability that $\mathcal{L}_{\mathcal{R}} < \mathcal{L}^{\rm obs}_{\mathcal{R}}$ for several choices of the region $\mathcal{R}$. If $\mathcal{R}$ is the entire $(x_{\rm DA}, y_{\rm DA})$ plane, the probability that $\mathcal{L}_{\mathcal{R}} < \mathcal{L}^{\rm obs}_{\mathcal{R}}$ is 7.8%. If $\mathcal{R}$ consists of the entire $(x_{\rm DA}, y_{\rm DA})$ plane, *except for* $x_{\rm DA} > 0.55$ and $y_{\rm DA} > 0.25$, the probability that $\mathcal{L}_{\mathcal{R}} < \mathcal{L}^{\rm obs}_{\mathcal{R}}$ is 50.2%, indicating that the data are in good agreement with the Standard Model in this region. In contrast, the probability that $\mathcal{L}_{\mathcal{R}} < \mathcal{L}^{\rm obs}_{\mathcal{R}}$ in the region $\mathcal{R}$ defined by $x_{\rm DA} > 0.55$ and $y_{\rm DA} > 0.25$ is 0.72%.

10 Conclusions

Using the ZEUS detector at HERA, we have studied the reaction $e^+p \to e^+X$ for $Q^2 > 5000\,{\rm GeV}^2$ with a 20.1 pb^{-1} data sample collected during the years 1994 to 1996.

For Q^2 below $15000\,{\rm GeV}^2$, the data are in good agreement with Standard Model expectations. For $Q^2 > 35000\,{\rm GeV}^2$, two events are observed while 0.145 ± 0.013 events are

expected. A statistical analysis of a large ensemble of simulated Standard Model experiments indicates that with probability 6.0%, an excess at least as unlikely as that observed would occur above *some* Q^2 cut.

For $x > 0.55$ and $y > 0.25$, four events are observed where 0.91 ± 0.08 events are expected. A statistical analysis which assigns a probability to the two-dimensional distribution of the events in x and y yields a probability of 0.72% for the region $x > 0.55$ and $y > 0.25$ and a probability of 7.8% for the entire $Q^2 > 5000\,\mathrm{GeV}^2$ data sample.

The observed excess above Standard Model expectations is particularly interesting because it occurs in a previously unexplored kinematic region.

Acknowledgements

We appreciate the contributions to the construction and maintenance of the ZEUS detector by many people who are not listed as authors. We thank the DESY computing staff for providing the data analysis environment. The HERA machine group is especially acknowledged for the outstanding operation of the collider. Finally, we thank the DESY directorate for strong support and encouragement.

References

[1] Future Physics at HERA, ed. G.Ingelman, A.De Roeck and R.Klanner, (DESY, Hamburg 1996), and references therein;
R.Cashmore et al., Phys. Reports **122** (1985) 275.

[2] ZEUS Collab., M.Derrick et al., Phys. Rev. Lett. **75** (1995) 1006.

[3] H1 Collab., S.Aid et al., Phys. Lett. **B379** (1996) 319.

[4] E.Derman, Phys. Rev. **D7** (1973) 2755;
G.Ingelman and R.Rückl, Phys. Lett. **B201** (1988) 369.

[5] G.Altarelli and G.Martinelli, Phys. Lett. **B76** (1978) 89.

[6] Particle Data Group, R.M. Barnett et al., Phys. Rev. **D54** (1996) 1.

[7] H.Plothow–Besch, PDFLIB User's Manual–Version 7.07, W5051 PDFLIB, 1996.12.09, CERN–PPE, and references therein;
Int. J. Mod. Phys. **A10** (1995) 2901.

[8] NMC Collab., M.Arneodo et al., Phys. Lett. **B309** (1993) 222, and references therein.

[9] CCFR Collab., P.Z.Quintas et al., Phys. Rev. Lett. **71** (1993) 1307.

[10] CDF Collab., F.Abe et al., Phys. Rev. Lett. **77** (1996) 438;
Phys. Rev. Lett. **77** (1996) 5336;
D0 Collab., S.Abachi et al., FERMILAB Conf. 96/280-E, Paper submitted to the XXVIII International Conference on High Energy Physics, Warsaw.

[11] J.Huston et al., Phys. Rev. Lett **77**(1996)444.

[12] ZEUS Collab., M.Derrick et al., Phys. Lett. **B293** (1992) 465;
ZEUS Collab., M.Derrick et al., Z. Phys. **C63** (1994) 391.

[13] ZEUS Collab., The ZEUS Detector, Status Report 1993, DESY 1993.

[14] M.Derrick et al., Nucl. Inst. Meth. **A309** (1991) 77;
A.Andresen et al., Nucl. Inst. Meth. **A309** (1991) 101;
A.Bernstein et al., Nucl. Inst. Meth. **A336** (1993) 23.

[15] N.Harnew et al., Nucl. Inst. Meth. **A279** (1989) 290;
B.Foster et al., Nucl. Phys. B (Proc. Suppl.) **32** (1993) 181;
B.Foster et al., Nucl. Inst. Meth. **A338** (1994) 254.

[16] J.Andruszków et al., DESY 92–066 (1992).

[17] LEPTO 6.5 with the matrix element plus parton shower option: G.Ingelman, in Physics at HERA, ed. W.Büchmuller and G.Ingelman (DESY, Hamburg 1991), vol. 3, 1366.

[18] HERACLES 4.5.2: A.Kwiatkowski, H.Spiesberger, and H.–J.Möhring, Physics at HERA, *ibid.*, vol. 3, 1294;
A. Kwiatkowski, H. Spiesberger, and H.-J. Möhring, Z. Phys. **C50** (1991) 165.

[19] DJANGO 1: G.Schuler and H.Spiesberger, Physics at HERA, *ibid.*, vol. 3, 1419.

[20] MRS: A.D.Martin, W.J. Stirling, and R.G. Roberts, Phys. Rev. **D50** (1994) 6734;
A.D. Martin, W.J. Stirling, and R.G. Roberts, Int. J. Mod. Phys. **A10** (1995) 2885.

[21] PYTHIA 5.7: T.Sjöstrand, Comp. Phys. Comm. **82** (1994) 74.

[22] ZEUS Collab., M.Derrick et al., Phys. Lett. **B322** (1994) 287.

[23] HERWIG 5.2: G.Marchesini et al., Comp. Phys. Comm. **67** (1992) 465.

[24] EPVEC: U.Baur, J.A.M.Vermaseren, and D.Zeppenfeld, Nucl.Phys. **B375** (1992) 3.

[25] ZLPAIR: A generator based on J.A.M. Vermaseren, Nucl. Phys. **B229** (1983) 347.

[26] GEANT 3.13: R. Brun et al., CERN DD/EE–84–1 (1987).

[27] S.Bentvelsen,J.Engelen, and P.Kooijman, Physics at HERA, *ibid.*, vol. 1, 23.

[28] W.Hollik et al., Physics at HERA, *ibid.*, vol. 2, 923.

[29] HECTOR: A. Arbuzov et al., DESY 95-185 (1995).

[30] ZEUS Collab., M.Derrick et al., Z. Phys. **C72** (1996) 399.

[31] NMC Collab., M.Arneodo et al., hep-ph/9610231, October 1996 (subm. to Nucl. Phys).

[32] L.W.Whitlow et al., Phys. Lett. **B282** (1992) 475.

[33] BCDMS Collab., A.C.Benvenuti et al., Phys. Lett. **B223** (1989) 485; Phys. Lett. **B237** (1990) 592.

[34] CTEQ: H.L. Lai et al. Phys. Rev. **D51** (1995) 4763.

[35] GRV: M. Glück, E. Reya, and A. Vogt,Z. Phys. **C67** (1995) 433.

ZEUS 1994-1996

$x_{\rm DA}^{\rm min}$ / $x_{\rm DA}^{\rm max}$	0.05 / 0.15	0.15 / 0.25	0.25 / 0.35	0.35 / 0.45	0.45 / 0.55	0.55 / 0.65	0.65 / 0.75	0.75 / 0.85	0.85 / 0.95
$0.95 < y_{\rm DA} < 1.00$	0.15	0.015	0.033	0.013	0.0055	0.0015	0.0012		
$0.85 < y_{\rm DA} < 0.95$	8.8 **9**	1.2 **3**	0.32	0.10	0.028 **1**	0.01	0.0034		
$0.75 < y_{\rm DA} < 0.85$	12 **16**	2.5 **4**	0.50 **1**	0.15	0.050	0.011	0.0039		
$0.65 < y_{\rm DA} < 0.75$	13 **10**	3.7 **3**	0.86	0.26	0.082	0.022	0.0054 **1**	0.0020	
$0.55 < y_{\rm DA} < 0.65$	15 **12**	6.1 **3**	1.65 **3**	0.46 **1**	0.15	0.046	0.0090	0.0024	
$0.45 < y_{\rm DA} < 0.55$	12 **6**	11 **13**	2.5 **1**	0.85	0.28	0.084 **1**	0.0208	0.0032	
$0.35 < y_{\rm DA} < 0.45$	4.6 **3**	18 **17**	5.5 **6**	1.75	0.52	0.16	0.0403	0.0093	
$0.25 < y_{\rm DA} < 0.35$		18 **23**	11 **6**	3.74 **7**	1.19 **1**	0.34 **2**	0.1104	0.0175	0.0066
$0.15 < y_{\rm DA} < 0.25$		2.2 **1**	14 **15**	9.6 **10**	3.32 **3**	1.2	0.2784 **1**	0.0717	0.0077
$0.05 < y_{\rm DA} < 0.15$				1.3 **1**	2.14 **3**	1.6 **2**	0.9052 **1**	0.3022 **1**	0.1216

Table 1: The observed numbers of events in bins of $x_{\rm DA}$ and $y_{\rm DA}$ (bottom number in each box), compared to the expected number of e^+p NC events (top number in each box). There are no events observed above $x_{\rm DA} = 0.95$.

ZEUS 1994-1996

Event Date	11-Oct-94	03-Nov-95	12-Sep-96	12-Oct-96	21-Nov-96
E_t [GeV]	123.	217.	193.	204.	187.
p_t [GeV]	8.9	8.2	2.9	2.2	10.2
$E - p_Z$ [GeV]	47.8	53.2	49.7	50.2	49.1
E_q [GeV]	67.4	235.	270.	151.	276.
$\gamma_{\rm raw}$	69.0°	28.1°	19.9°	40.7°	19.7°
E'_e [GeV]	324.	220.	149.	366.	134.
θ_e	11.9°	27.8°	39.3°	15.4°	41.1°
$(x_{\rm DA})_{\rm raw}$	0.468	0.541	0.535	0.668	0.515
$(y_{\rm DA})_{\rm raw}$	0.868	0.503	0.330	0.733	0.316
$(Q^2_{\rm DA})_{\rm raw}$ [$10^4\,{\rm GeV}^2$]	3.67	2.45	1.59	4.42	1.47
γ	67.6°	26.7°	17.3°	38.6°	17.0°

Table 2: Measured variables for the five events selected as described in the text. The first row shows the date the event was acquired. The following rows indicate the quantities defined in equations 7 and 8, followed by the energy and angle of the scattered positron. The values of x, y, and Q^2 calculated from $\gamma_{\rm raw}$ and θ_e are shown next. The last row shows the γ angle.

ZEUS 1994-1996

Event Date	11-Oct-94	03-Nov-95	12-Sep-96	12-Oct-96	21-Nov-96
$x_{\rm DA}$	0.480	0.570	0.617	0.709	0.597
$\delta x_{\rm DA}$	0.035	0.029	0.054	0.034	0.053
$y_{\rm DA}$	0.865	0.490	0.299	0.721	0.285
$\delta y_{\rm DA}$	0.008	0.010	0.017	0.008	0.017
$Q^2_{\rm DA}$ $[10^4\,{\rm GeV}^2]$	3.75	2.52	1.66	4.61	1.54
$\delta Q^2_{\rm DA}$ $[10^4\,{\rm GeV}^2]$	0.26	0.07	0.05	0.16	0.04
x_e	0.525	0.536	0.562	0.605	0.443
δx_e	0.048	0.048	0.102	0.060	0.063
y_e	0.854	0.505	0.319	0.752	0.350
δy_e	0.018	0.024	0.039	0.021	0.032
Q^2_e $[10^4{\rm GeV}^2]$	4.05	2.44	1.62	4.10	1.40
δQ^2_e $[10^4{\rm GeV}^2]$	0.31	0.11	0.09	0.30	0.07

Table 3: Kinematic variables for the five events selected as described in the text. The first six lines below the event dates show the double angle values and their estimated uncertainties. These include the r. m. s. errors as well as small contributions from the uncertainties associated with the correction procedure. The last block of six lines shows the kinematic variables reconstructed from the energy and the angle of the positron. These latter errors are dominated at present by systematic uncertainties associated with the positron energy measurement.

Background Process	cross section [fb]	
	$x_{\rm DA} > 0.45$	$x_{\rm DA} > 0.55$
$\gamma p \to \gamma X$	0.28	0.28
$\gamma p \to$ dijets	< 1.8	< 1.8
$ep \to e\gamma X$	< 0.2	< 0.2
$\gamma\gamma \to \ell\ell$	< 0.1	< 0.1
$W \to e\nu$	< 0.5	< 0.5
Expected NC DIS	165	46

Table 4: Expected cross sections for different background processes in the regions ($x_{\rm DA} > 0.45, y_{\rm DA} > 0.25$) and ($x_{\rm DA} > 0.55, y_{\rm DA} > 0.25$). The expected numbers of background events are obtained by multiplying these cross sections with the integrated luminosity of $0.02\,{\rm fb}^{-1}$. The quoted limits are at 90% CL. Shown for comparison in the last row are the cross sections expected for e^+p NC events.

Systematic errors	
fixed-target experimental uncertainties	± 0.062
$0.113 < \alpha_s < 0.123$	± 0.019
overall assumed r. m. s. uncertainty	± 0.065
Cross checks	
$10\% <$ strange fraction $< 30\%$	< 0.001
uncertainties in charm evolution	< 0.005
GRV94, MRSA, CTEQ3 comparison	± 0.020
GRV94 NLO versus LO	$+0.010$
High-x gluon (CDF inspired, CTEQ4 HJ)	$+0.019$

Table 5: Relative uncertainties in the integrated cross section for $x > 0.5$ and $y > 0.25$ due to variations in the structure functions. The top two entries represent the two dominant contributions to these uncertainties, and so provide the systematic error, shown in the third row,which is used in this paper. The remaining entries are cross checks that are not independent of the items in the first two rows.

ZEUS 1994-1996

$Q^{2*}_{\rm DA}$ [GeV^2]	$N_{\rm obs}(Q^2_{\rm DA} > Q^{2*}_{\rm DA})$	μ	$\delta\mu$
5000	191	196.5	± 9.87
10000	33	32.18	± 2.04
15000	12	8.66	± 0.66
20000	5	2.76	± 0.23
25000	3	1.01	± 0.09
30000	2	0.37	± 0.04
35000	2	0.145	± 0.013

Table 6: The observed and expected numbers of events above various $Q^2_{\rm DA}$ thresholds. The first two columns give $Q^{2*}_{\rm DA}$, the lower limit on $Q^2_{\rm DA}$, and $N_{\rm obs}$, the number of observed events with $Q^2_{\rm DA} > Q^{2*}_{\rm DA}$. The next two columns give μ, the expected number of events with $Q^2_{\rm DA} > Q^{2*}_{\rm DA}$, and $\delta\mu$, the uncertainty on μ, which includes uncertainties in the cross section prediction as well as experimental uncertainties.

ZEUS 1994-1996

$y_{\rm DA}$ range	$\mathcal{P}_{\rm min}(x^*_{\rm DA})$	$x^*_{\rm DA}$	$N_{\rm obs}(x_{\rm DA} > x^*_{\rm DA})$	μ	$P_{\rm SM}$
$y_{\rm DA} > 0.05$	1.61%	0.708	4	0.95	16.0%
$y_{\rm DA} > 0.15$	2.57%	0.708	2	0.25	23.0%
$y_{\rm DA} > 0.25$	0.60%	0.569	4	0.71	7.2%
$y_{\rm DA} > 0.35$	3.38%	0.708	1	0.034	26.6%
$y_{\rm DA} > 0.45$	1.32%	0.569	2	0.17	12.7%
$y_{\rm DA} > 0.55$	0.96%	0.708	1	0.010	9.5%
$y_{\rm DA} > 0.65$	0.50%	0.708	1	0.005	5.0%

Table 7: Minimal Poisson probabilities associated with the $x_{\rm DA}$ distributions for different $y_{\rm DA}$ cuts. The columns labelled $\mathcal{P}_{\rm min}(x^*_{\rm DA})$ and $x^*_{\rm DA}$ give the minimal probability and the cut on $x_{\rm DA}$ where it occurs. The next two columns give $N_{\rm obs}$ and μ, the number of events observed and the number expected with $x_{\rm DA} > x^*_{\rm DA}$. The column labelled $P_{\rm SM}$ gives the probability that a simulated e^+p Standard Model experiment yields a lower value of $\mathcal{P}_{\rm min}(x^*_{\rm DA})$ than the one observed. All values are for $Q^2_{\rm DA} > 5000\,{\rm GeV}^2$.

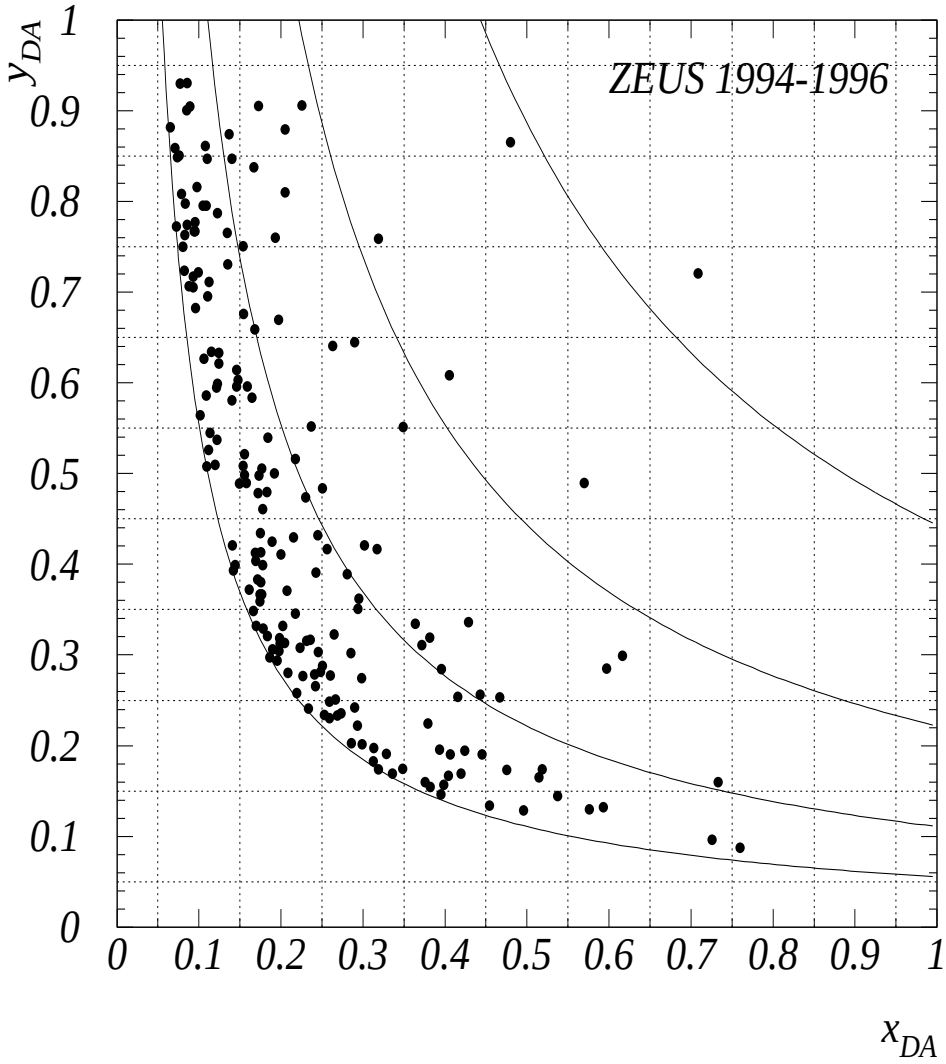

Figure 1: The distribution of the event sample in $x_{\rm DA}$ and $y_{\rm DA}$. The lines indicate constant values of $Q^2_{\rm DA} = x_{\rm DA} y_{\rm DA} s$ for $Q^2_{\rm DA} = 5000$, 10000, 20000 and 40000 GeV^2.

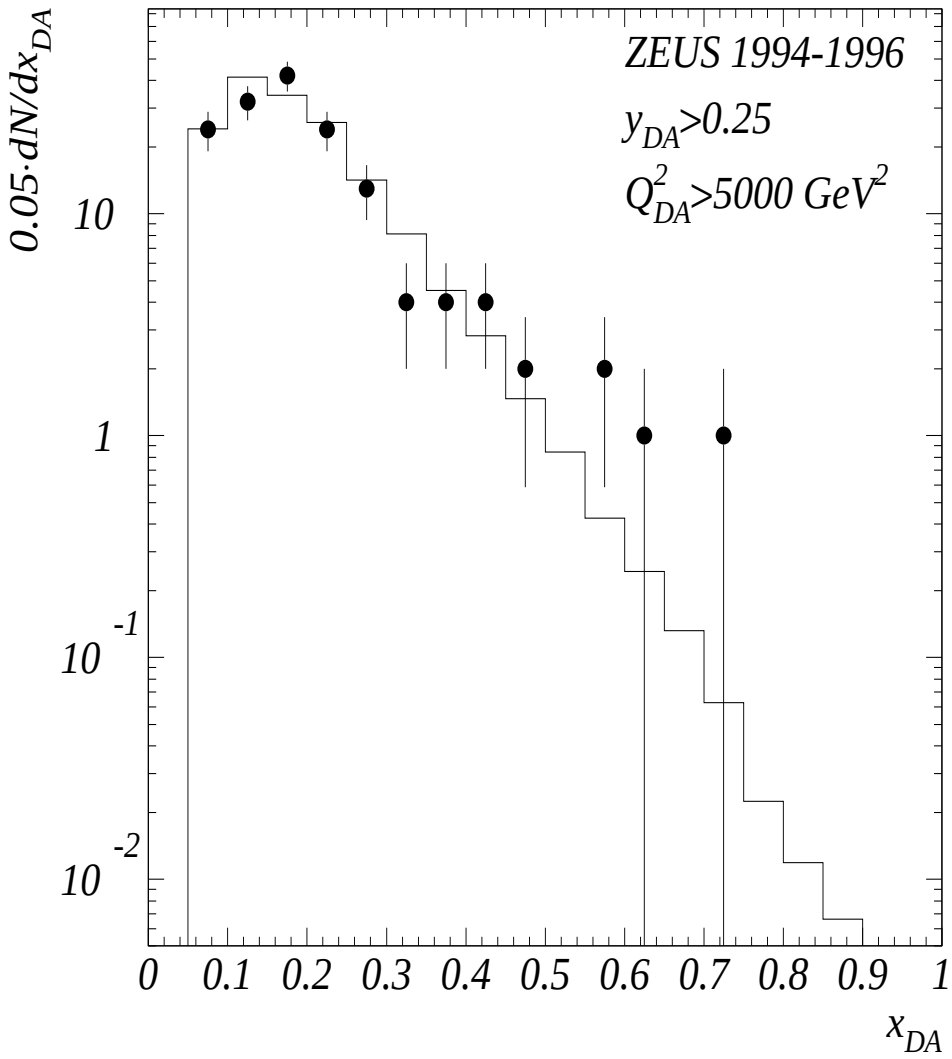

Figure 2: The $x_{\rm DA}$ distribution of the observed events with the cuts shown (full dots), compared to the Standard Model e^+p NC expectation (histogram). The error bars on the data points are obtained from the square root of the number of events in the bin.

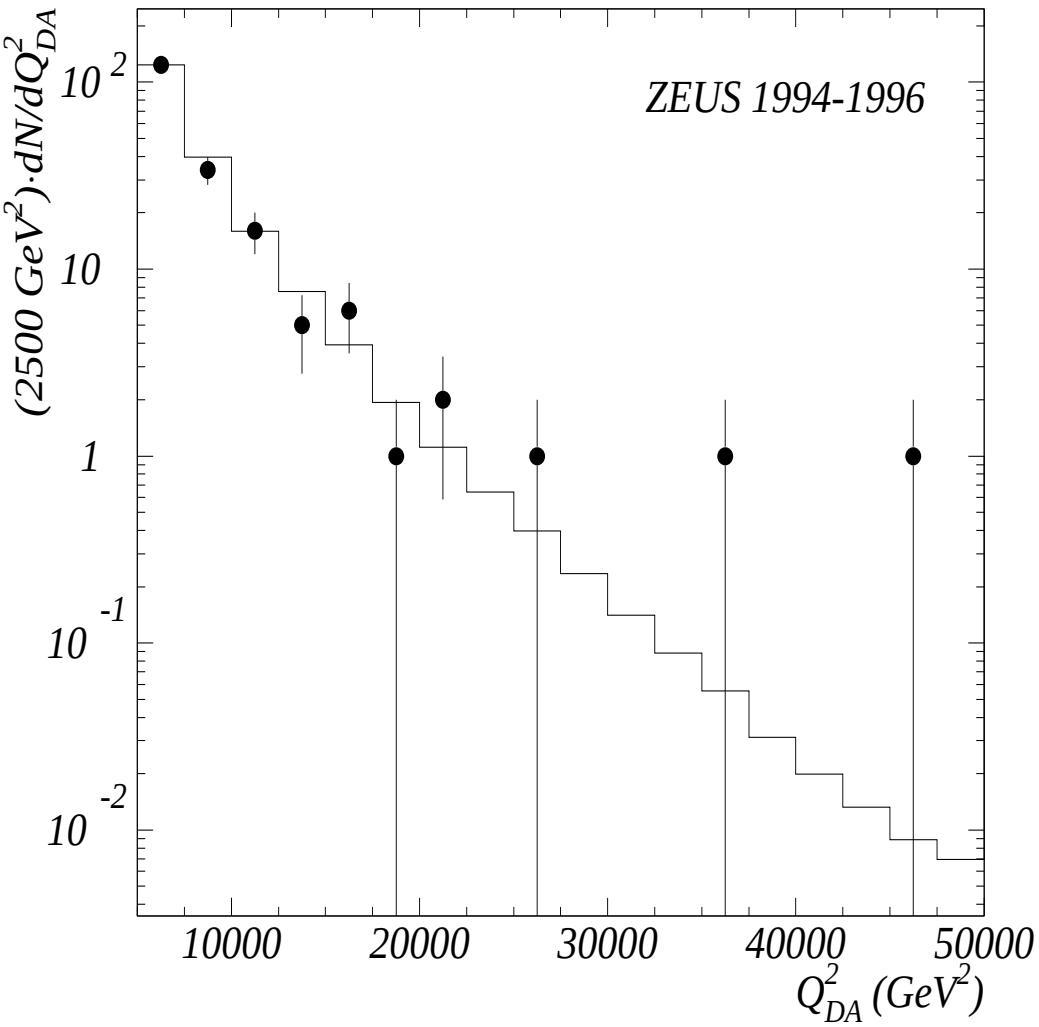

Figure 3: The $Q^2_{\rm DA}$ distribution of the observed events (full dots), compared to the Standard Model e^+p NC expectation (histogram). The error bars on the data points are obtained from the square root of the number of events in the bin.

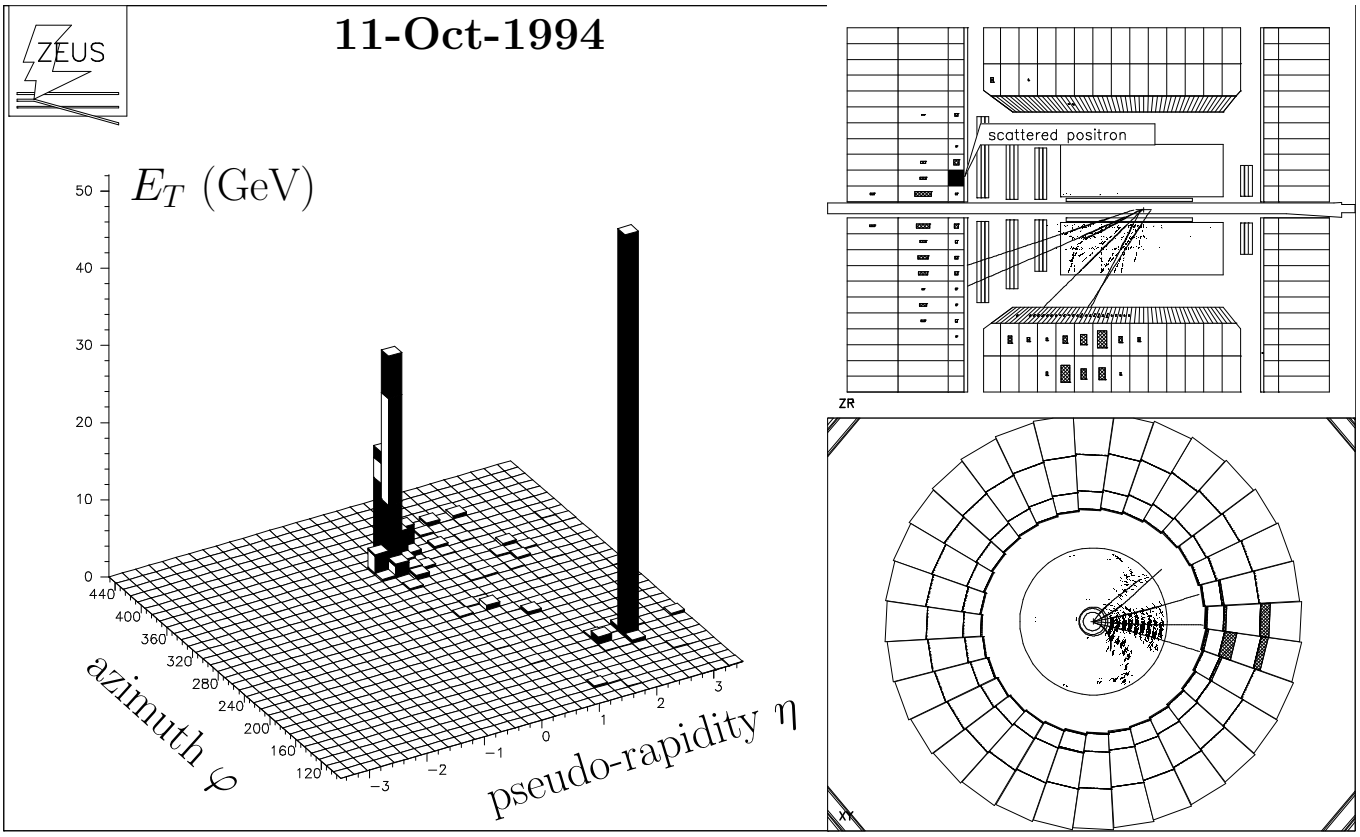

Figure 4: A display of the high Q^2 event recorded on 11-Oct-94. The top right part shows the ZEUS inner tracking system and the calorimeter. The filled rectangles in the calorimeter denote energy deposits which are above the noise thresholds described in the text (cf. Section 3.1). The bottom right display shows a projection onto a plane perpendicular to the beam axis, where only BCAL energy deposits are shown. The left part of the figure shows the calorimeter transverse energy deposits. This display demonstrates that the scattered positron is well isolated.

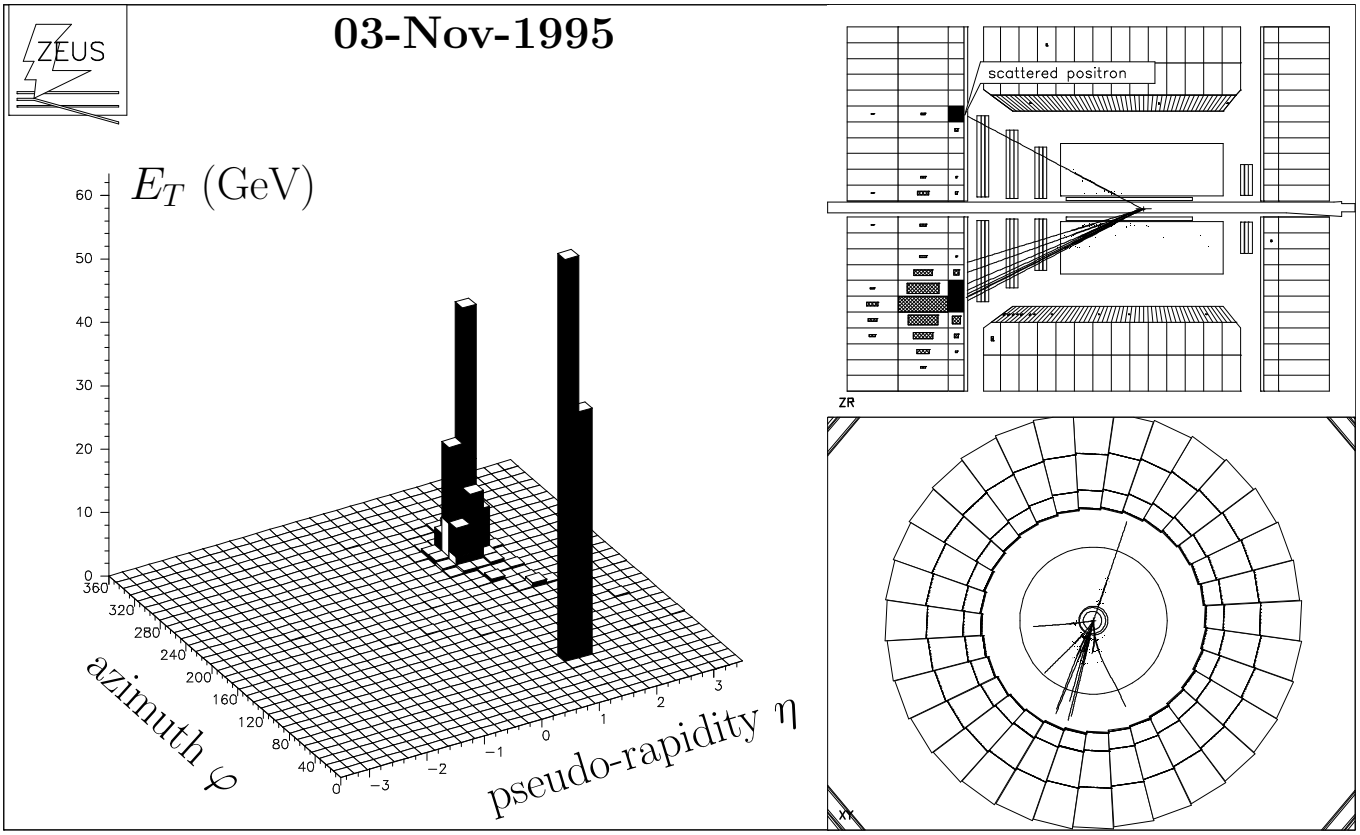

Figure 5: A display of the high Q^2 event recorded on 03-Nov-95. The description of the display is identical to the previous figure. However, for this event the positron polar angle θ_e is large enough to be in the CTD acceptance.

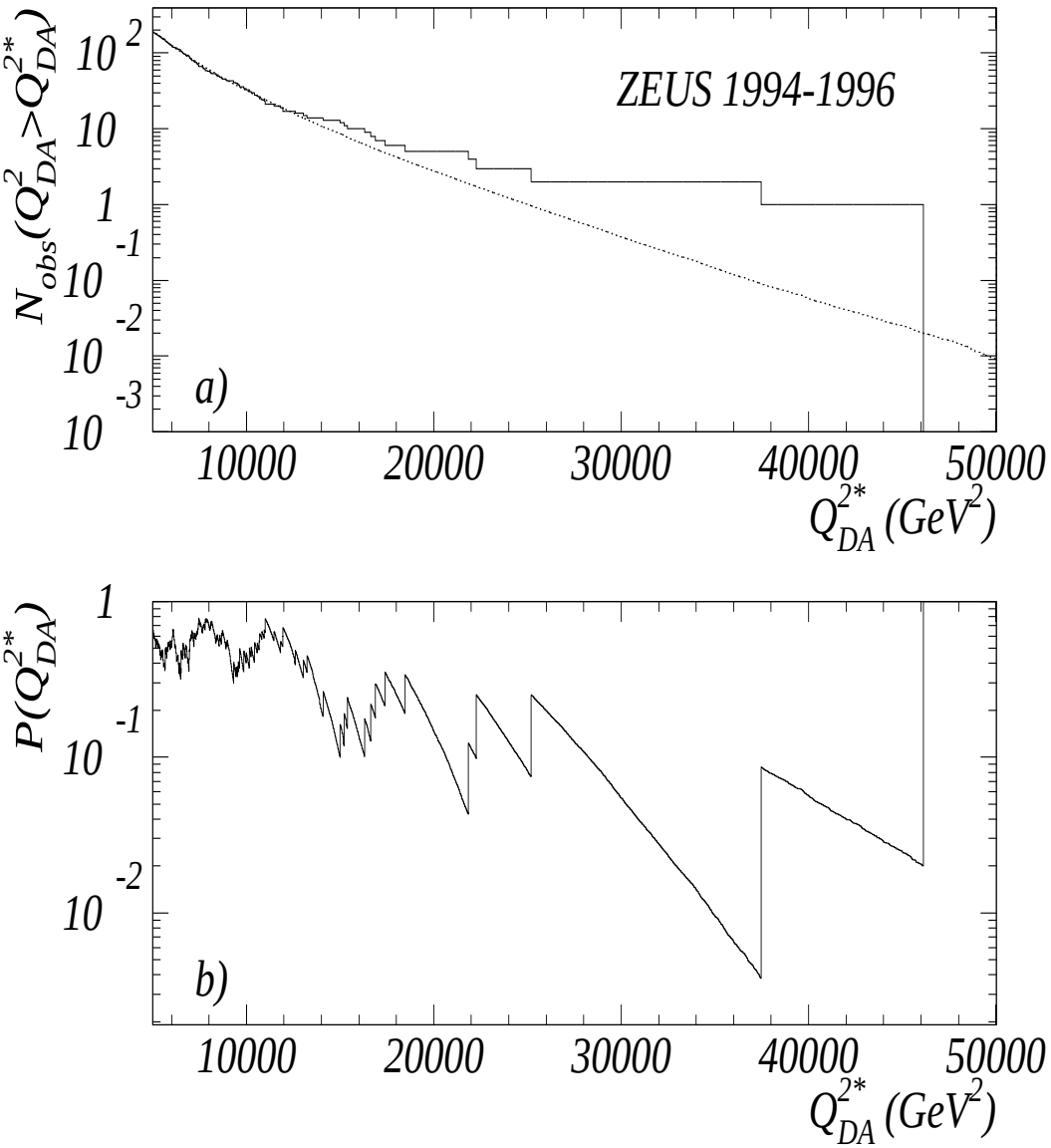

Figure 6: In (a), the solid line indicates the number of observed events with $Q^2_{\rm DA} > Q^{2*}_{\rm DA}$ as a function of $Q^{2*}_{\rm DA}$. The dotted line indicates the number of events expected from e^+p NC DIS with $Q^2_{\rm DA} > Q^{2*}_{\rm DA}$. In (b) is shown the Poisson probability (eqn. 11) to observe at least as many events as were observed with $Q^2_{\rm DA} > Q^{2*}_{\rm DA}$ as a function of $Q^{2*}_{\rm DA}$.

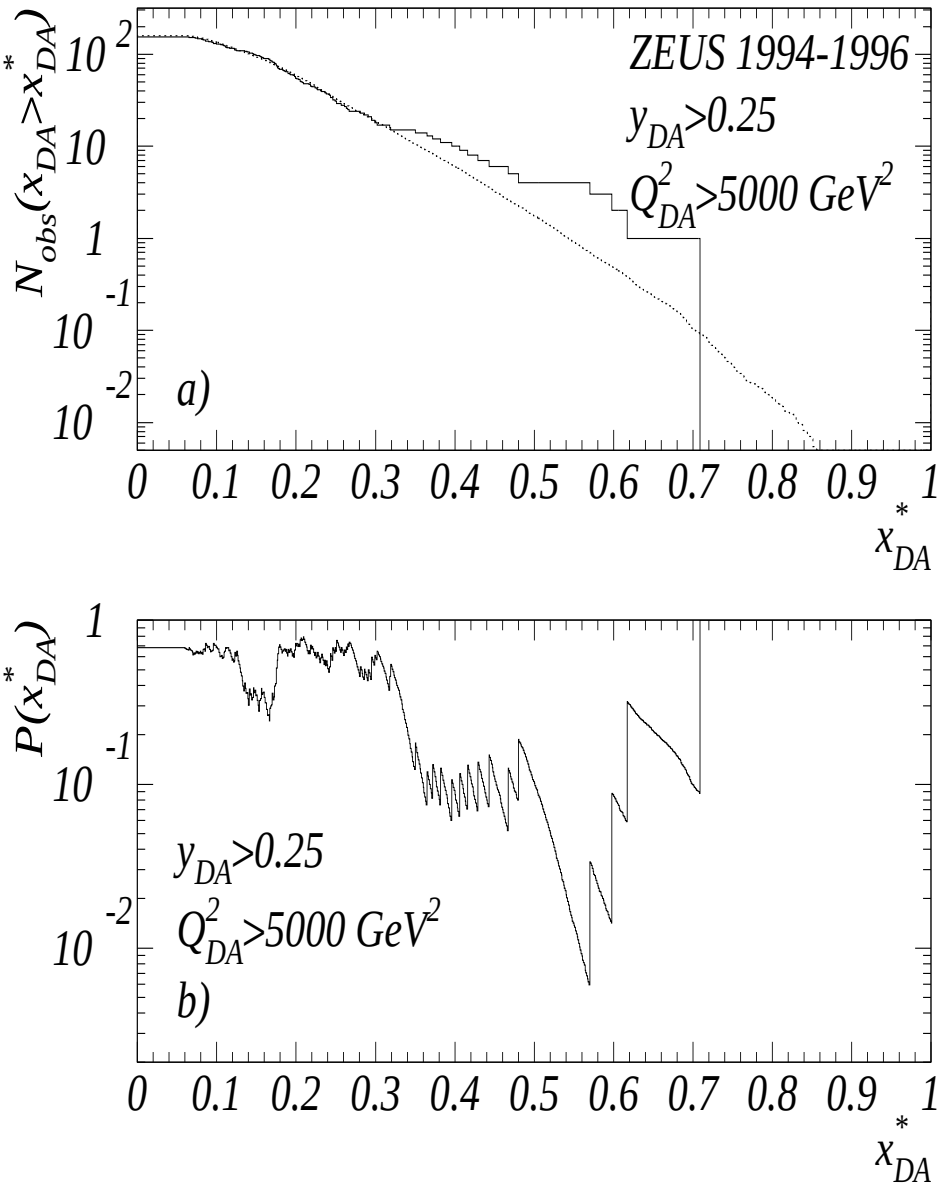

Figure 7: In (a), the solid line indicates the number of events observed with $y_{\rm DA} > 0.25$ and $x_{\rm DA} > x^*_{\rm DA}$ as a function of $x^*_{\rm DA}$. The dotted line indicates the number of expected e^+p NC DIS events with $y_{\rm DA} > 0.25$ and $x_{\rm DA} > x^*_{\rm DA}$. In (b) is shown the Poisson probability (eqn. 11) to observe at least as many events as were observed with $x_{\rm DA} > x^*_{\rm DA}$ as a function of $x^*_{\rm DA}$.